Clays and Clay Minerals (2024), **72**, e21, 1–12
doi:10.1017/cmn.2024.17

Original Paper

Millennial-scale paleoclimate changes recorded in Holocene ferromanganese crusts with oscillatory micro-bands: insights from mineralogical and chemical variations in hydrogenetic ferromanganese crusts of the Magellan Seamounts

Seungyeol Lee[1,2] and Huifang Xu[1]

[1]Department of Geoscience, University of Wisconsin-Madison, Madison, WI 53706, USA and [2]Department of Earth and Environmental Sciences, Chungbuk National University, Cheongju 28644, Republic of Korea

Abstract

This study investigates the hydrogenetic ferromanganese crust (HFMC) from the Magellan Seamounts in the northwest Pacific Ocean, focusing on its mineralogy, crystal chemistry, and paleoclimatic records. Given that ferromanganese is composed of poorly crystalline MnOx phases, such as vernadite, structural determination using conventional X-ray diffraction (XRD) methods is challenging and has very limited effectiveness. Therefore, synchrotron-based pair-distribution function (PDF) analysis of total X-ray scattering and high-resolution electron microscopy techniques were employed to characterize the structures and compositions of HFMC. The results from the synchrotron XRD and transmission electron microscopy (TEM) reveal that the studied HFMC consists primarily of poorly crystalline Fe-bearing vernadite. The chemical analysis of the HFMC layers indicates that the rare-earth elements (REE) and P were preferentially adsorbed on the Fe-rich vernadite, whereas platinum-group elements (PGE), Co, and Ni were enriched in the Mn-rich vernadite. The top layers of the HFMC display fine-scale compositional variations (cycle of ~1600 y) that signify millennial-scale paleoclimate oscillations during the Middle-Late Pleistocene and Holocene periods linked to the glacial termination event that occurred ~126,000 y ago. This millennial-scale oscillation correlates with sea-level variations influenced by the expansion and contraction of ice sheets, offering a crucial signal for understanding the paleoclimatic interpretation throughout the glacial periods. To fully decipher the fine-scale paleoclimate signals and assist in forecasting future climatic conditions, a more extensive examination of ferromanganese crusts from diverse depths, sources, and locations is necessitated.

Keywords: glacial termination; hydrogenetic ferromanganese crust; millennial-scale paleoclimatic oscillations; rare-earth elements; vernadite

(Received: 21 October 2023; revised: 19 February 2024; accepted: 25 April 2024)

Introduction

Hydrogenetic ferromanganese crust (HFMC) occurs worldwide on seamounts, ridges, and plateaus formed by the direct precipitation of seawater on the surface of rock substrates (e.g. breccia, basalt, phosphorite, and limestone) or sediments on the seafloor (Hein et al., 2000; Jiang et al., 2011; Hein et al., 2013). The HFMC is considered to be a prospective resource for critical metals (e.g. Ni, Co, Zn, Ti, Li, etc.), rare-earth elements (REE), and platinum-group elements (PGE) (Bolton et al., 1986; Cronan, 1999; Hein et al., 2000; Hein et al., 2013). The HFMC is mostly composed of ferruginous vernadite (δ-MnO_2) nanophase (Bolton et al., 1986; Cronan, 1999), and trace element ions can be adsorbed onto the vernadite nanophase with outer-sphere or inner-sphere sorption (Hein and Koschinsky, 2014; Manceau et al., 2014; Grangeon et al., 2017). Redox conditions, sea level, current activity, seawater composition, and deep-sea circulation all affect how HFMC forms and what it is made of (Turney et al., 2004; Glasby et al., 2007; Berezhnaya et al., 2018). The HFMC is found at depths of ~400–5500 m and has large specific surface areas (200–600 m^2 g^{-1}) with growth rates of 1–10 mm Myr^{-1} (Cronan, 1999; Glasby et al., 2007; Hein and Koschinsky, 2014; Marino et al., 2018). Due to the slow growth rates, HFMC can represent condensed stratigraphic sections that preserve paleoceanographic conditions (Cronan, 1999; Frank et al., 1999; Hein et al., 2000; Koppers et al., 2001; Glasby et al., 2007).

The HFMC in the Magellan Seamounts was developed on guyots, which are located in the Eastern Mariana basin of the Pacific Ocean (Smith et al., 1989; Lee et al., 2019). The geological setting, geochemistry, and mineralogy of HFMC in the Magellan Seamounts have been studied widely for their potential as future mineral resources (Hein et al., 2000; Pan et al., 2005; Yang et al., 2019a).

Corresponding authors: Seungyeol Lee and Huifang Xu; Emails: slee2@cbnu.ac.kr; hfxu@geology.wisc.edu

Cite this article: Lee S., & Xu H. (2024). Millennial-scale paleoclimate changes recorded in Holocene ferromanganese crusts with oscillatory micro-bands: insights from mineralogical and chemical variations in hydrogenetic ferromanganese crusts of the Magellan Seamounts. *Clays and Clay Minerals* **72**, e21, 1–12.
https://doi.org/10.1017/cmn.2024.17

On the Magellan Seamounts, exploratory projects are being carried out by several countries (Du et al., 2018). Previous studies have accomplished geological dating of the Magellan HFMC based on ^{10}Be-dating, Co-geochronometry, and planktonic/benthic foraminiferal assemblages (Koppers et al., 1998; Cheng et al., 2005; Glasby et al., 2007; Ren et al., 2007; Melnikov and Pletnev, 2013). The Magellan Seamounts began forming as submarine volcanoes during the Cretaceous (Smith et al., 1989; Koppers et al., 2001; Glasby et al., 2007). The stratigraphic analysis of Magellan HFMC revealed four main layers from the bottom (Late Paleocene) to the top (Pliocene-Quaternary) (Glasby et al., 2007). Variations in paleoceanographic conditions with geological boundaries were recorded in the stratigraphic sections of the HFMC (Koppers et al., 1998; Glasby et al., 2007).

This work focuses on a thorough analysis of the HFMC using a variety of high-resolution methods, such as transmission electron microscopy (TEM), scanning electron microscopy (SEM), electron microprobe analysis (EPMA), pair-distribution function (PDF) analysis of total X-ray scattering, and synchrotron X-ray diffraction (XRD). These cutting-edge techniques make it possible to characterize the atomic structures of poorly crystallized nano-minerals within ferromanganese crusts, as well as providing insights into the enrichment processes of trace elements and paleoclimate indicators. The techniques and discoveries from this study provide valuable insights into the research of the ferromanganese crust and other deep-sea mineral deposits.

Materials and methods

Hydrogenetic ferromanganese crust

The HFMC sample (no. 0327, latitude 15°54′N and longitude 163° 12′E, water depth 2149.5 m; see Fig. S1 in the Supplementary material) was collected from the Magellan Seamounts in the northwest Pacific Ocean by the DY105-13 cruise of the vessel *Haiyang*. The HFMC sample shows a dark brown to black color with micro-laminations and columnar growth on the botryoidal surface (Fig. 1; see also Fig. S2 in the Supplementary material). Late-stage goethite (orange) and fluorapatite (white) fill in the pores and fractures (Fig. 1; see also Fig. S3 in the Supplementary material). The amounts of the major elements and REE in the HFMC sample are presented in Tables S1 and S2 in the Supplementary material. The range of the studied HFMC sample's total REE concentration is 1244–2388 ppm (n = 24), with an average value of 1624 ppm in the outer part; 937–2804 ppm (n = 30), with an average value of 1422 ppm in the middle; and 161–841 ppm (n = 21), with an average value of 455 ppm in the inner part. Additionally, previous studies have reported on the REE geochemistry, the enrichment process of PGE, and the noble gas isotopic compositions of the studied HFMC sample (Xue et al., 2005; Sun et al., 2006; Sun et al., 2007; Xue, 2007; Zhang et al., 2009).

Experimental methods

The shiny and fragile black vernadite grains were collected from within the HFMC sample. The samples were crushed gently just before the experiment in order to make them suitable for powder analysis. The multi-point Brunauer–Emmett–Teller (BET) surface areas and Barrett–Joyner–Halenda (BJH) pore-size distributions of the HFMC samples were determined by the N_2-adsorption technique using a Nova 4200e surface area and pore-size analyzer (Quantachrome Instruments, FL, USA) at the Geoscience Department, University of Wisconsin-Madison. Finely ground powders were placed inside polyimide tubes with an inner diameter of 1 mm for the XRD and PDF measurements. The

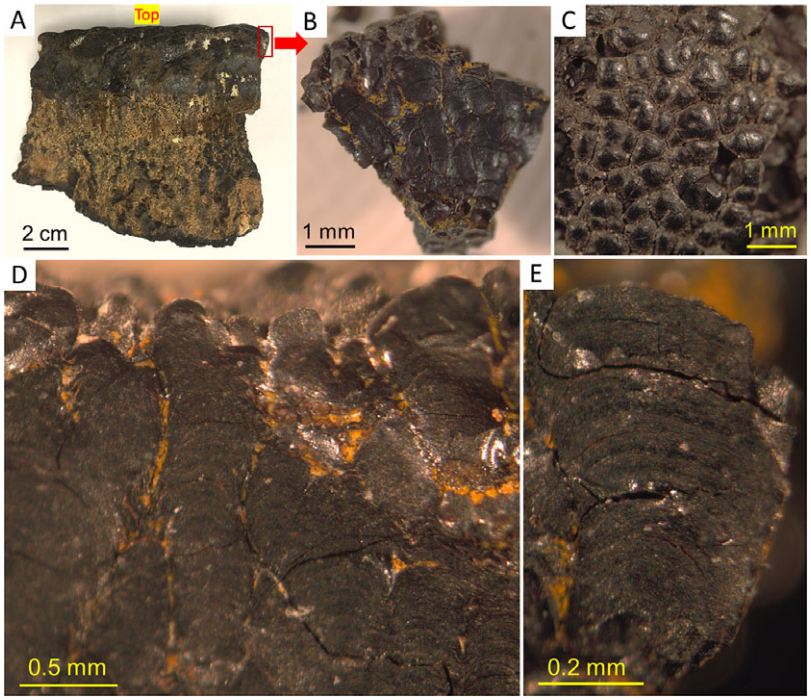

Figure 1. Photographs of hydrogenetic Fe-Mn crust collected from Magellan Seamounts in the northwest Pacific Ocean, showing black laminations with columnar growth structures and botryoidal surfaces. Late-stage goethite and fluorapatite fill in the pores and fractures. (A) Hand specimen; (B) side view of the area outlined; (C) top view showing the botryoidal surface; (D) surface of a cross-section showing the columnar growth structure; (E) enlarged view of a columnar structure.

https://doi.org/10.1017/cmn.2024.17 Published online by Cambridge University Press

powder XRD data were collected with a two-dimensional (2D) image-plate detector using a Rigaku Rapid II instrument (Rigaku Corporation, Tokyo, Japan) using Mo Kα radiation at the Geoscience Department, University of Wisconsin-Madison. 2D diffraction patterns were converted to conventional 2θ *vs* intensity XRD plots using the Rigaku 2DP software.

Synchrotron radiation PDF was conducted using X-rays (λ=0.24116 Å) on beamline 17-BM at the Advanced Photon Source (APS), Argonne National Laboratory, Illinois, USA. An amorphous Si area detector was utilized to gather 2D diffraction data in transmission geometry. Each individual exposure on the area detector was set to 1 s. This 1 s exposure was repeated 120 times, resulting in a total collection time of 120 s for each sample. The distance from the sample to the detector and the position of the beam center were calibrated using an LaB_6 standard. Diffraction data on empty polyimide tubing were collected for background subtraction during data reduction. *GSASII* software (Toby and Von Dreele, 2013) was used to integrate and convert the 2D pattern to 1D intensity *vs* wave vector (*Q*). The data obtained up to a Q_{max} of 19.6 $Å^{-1}$ were then transformed into PDF patterns using *PdfGetX3* (Juhás et al., 2013). PDF fitting and refinement were carried out using the *PDFGui* program (Farrow et al., 2007).

Samples for SEM and EPMA analysis were mounted onto glass slides, polished, and coated with carbon (~10 nm). Images of backscattered electrons (BSE) and elemental maps were obtained using a Hitachi S3400N (Hitachi, Tokyo, Japan) variable pressure SEM with an X-ray energy-dispersive spectroscopy (EDS) system at the Geoscience Department, University of Wisconsin-Madison. SEM analysis was performed in high-vacuum mode. The working distance of detectors from the specimen was set to 10 mm and an accelerating voltage of 15 kV was applied for both BSE images and elemental mapping. WDS EPMA measurements were made with the UW-Madison Cameca SX51 electron microprobe (Cameca, USA) at an accelerating voltage of 20 kV. Comprehensive quantitative analyses, which included the use of mineral standards, background subtraction, and matrix correction, were conducted utilizing the Probe for Windows-Enterprise software. TEM samples were prepared by depositing a suspension of crushed grains on a lacy carbon-coated Cu grid. All the TEM images and the selected-area electron diffraction (SAED) patterns were carried out using a Philips CM200-UT transmission microscope (ThermoFisher Scientific, USA) operated at 200 kV at the Materials Science Center, University of Wisconsin-Madison. The chemical composition by TEM was obtained using energy-dispersive X-ray spectra (EDS) with a Li-drifted Si detector. X-ray EDS spectra were collected using electron beams with a diameter of ~50 nm. Precautions were taken to prevent beam damage that could potentially modify the structure of vernadite.

Results and Discussion

Mineralogy

Hydrogenetic ferromanganese crust consists mainly of vernadite; on the other hand, diagenetic and hydrothermal crust commonly show the presence of birnessite, todorokite, asbolane, and buserite (Cronan, 1999). Powder XRD patterns were collected from the black manganese phases, from the inner part to the outer part of HFMC. These XRD patterns indicate a pure vernadite nanophase with broad diffraction peaks at 2.43, 1.41, and 1.22 Å (Fig. 2). Previous studies determined the crystal structure of synthetic vernadite (δ-MnO_2) (Zhu et al., 2012; Manceau et al., 2013) and natural vernadite (Lee et al., 2019) using synchrotron X-ray diffraction and scattering techniques. A weak and broad (001) peak together with strong (*hk*) diffraction peaks indicates thin layers of vernadite (i.e. nanosheets or 2D crystals) (Fig. 2). The increasing intensity of the (001) diffraction peak from the outer to inner part suggests the improved crystallinity of vernadite and/or multiple repetitions along the stacking direction or ***c*** axis (Fig. 2). The ratio of the *d* spacing of the first two main diffraction peaks is ~1.723 (i.e. 2.43/1.41), close to $\sqrt{3}$, suggesting pseudo-hexagonal symmetry in the manganese octahedral layer.

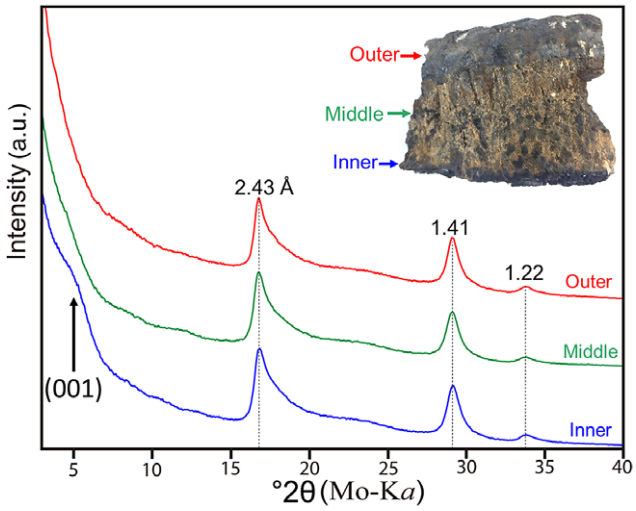

Figure 2. Powder XRD patterns of the HFMC from the outer part to the inner part, including an image of the sample specimen. The broad (001) diffraction peak indicates thin layer nanophases along the *c* axis.

HFMC samples were studied through the BET surface area and BJH pore-size distribution analyses to determine the nanopore structures of the vernadite phase (Fig. 3). The multi-point BET surface areas of the inner part, middle part, and outer part were 376, 404, and 421 $m^2\ g^{-1}$, respectively. The outer layers of HFMC have slightly larger surface areas than the inner portion, consistent with the outer layers having more poorly crystallized minerals due to their young-stage precipitates. The BJH pore-size distribution analyses revealed that the surface areas were dominated by nanopore surfaces (pore diameter <10 nm) (Fig. 3A). The BET surface area and BJH pore-size distribution analyses show a similar trend with hydrogenetic ferromanganese crusts from other seamounts in the northwest Pacific Ocean (Hein et al., 2000; Hein and Koschinsky, 2014).

TEM and combined EDS analyses provide information about the structure and chemistry of the vernadite nanophase in the HFMC (Fig. 4). Vernadite appears as aggregates of nanosized 2D crystals and the SAED pattern shows two broad diffraction rings at ~2.4 and ~1.4 Å (Fig. 4A), indicating the low crystallinity of vernadite. Natural vernadite nanophases showed the mixture component of ~7.2 Å vernadite and ~9.6 Å vernadite and interstratified phases are shown in Fig. S4 of the Supplmentary material (Lee et al., 2019). The lattice fringes of vernadite are mostly curved and curled (Fig. 4; see also Fig. S4 in the Supplementary material). The curved layers were caused by the presence of vacancies and/or substitutions of other cations in Mn layers, which is associated with a high concentration of defects in the vernadite structure (Zhu et al., 2012; Yang et al., 2018). TEM-EDS spectra indicate that the vernadite nanophase contains Na,

https://doi.org/10.1017/cmn.2024.17 Published online by Cambridge University Press

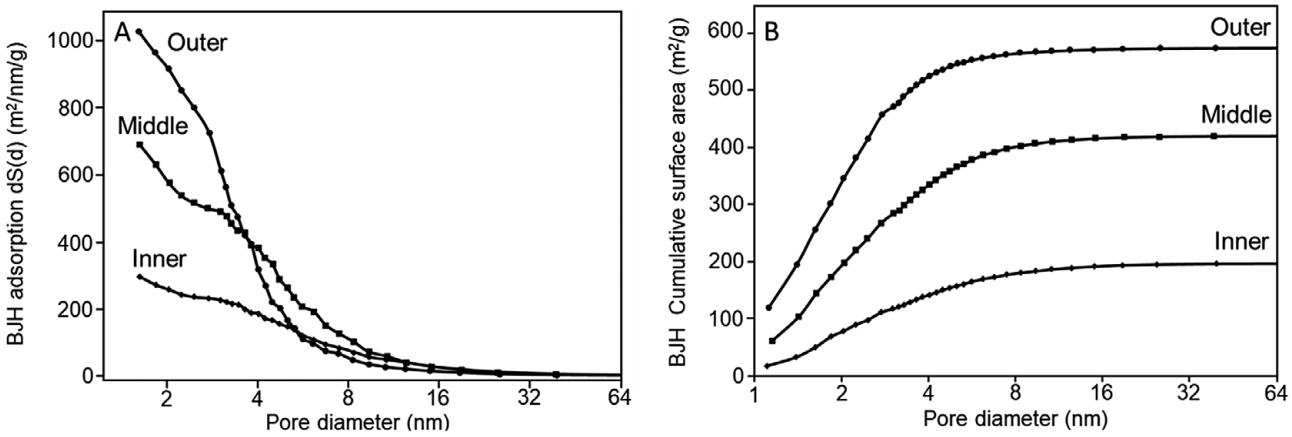

Figure 3. Diagrams illustrating nanopore-size distribution determined by Barrett-Joyner-Halenda BJH adsorption (A) and cumulated surface areas (B) for HFMC samples from the inner part to the outer part.

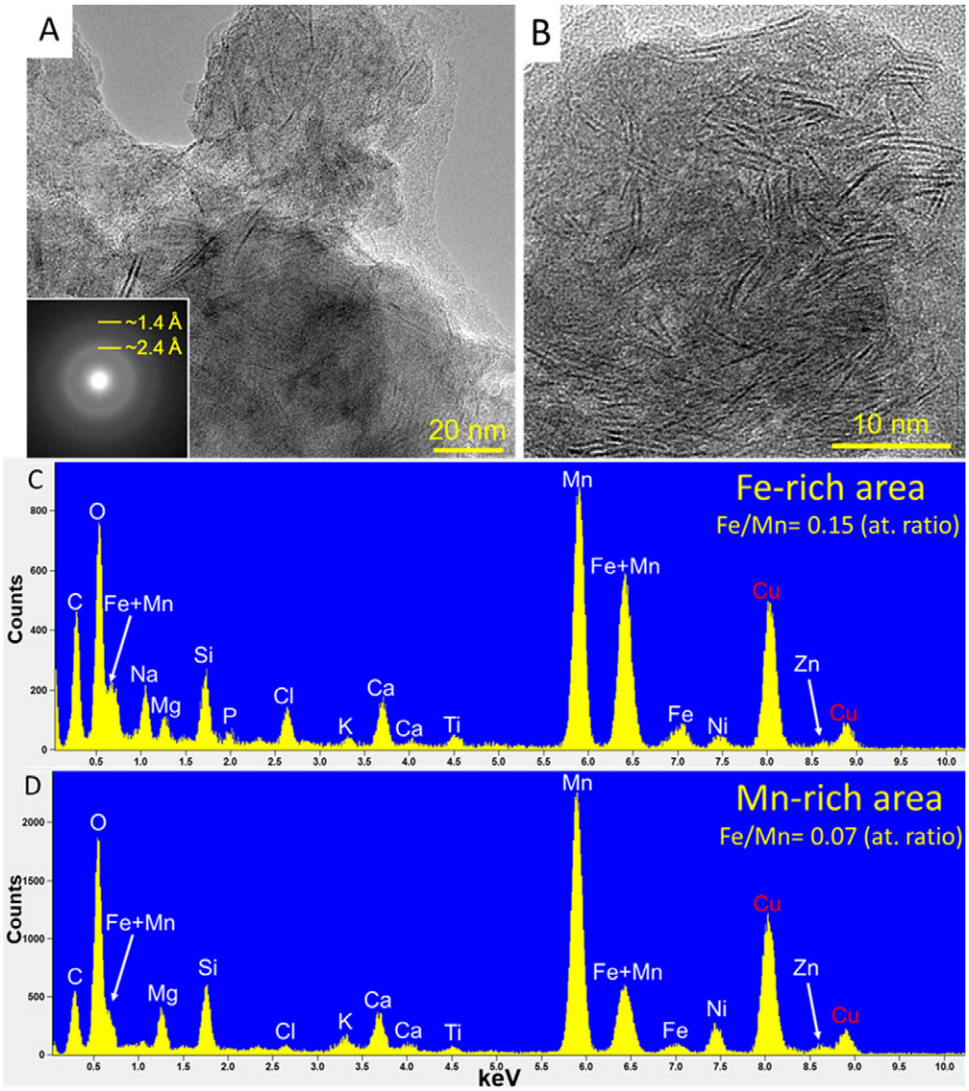

Figure 4. (A,B) Bright-field TEM images of vernadite nanophases from HFMC. Only the nanocrystals or flakes with (001) plane nearly parallel to the electron beam, show their lattice fringes. Inserted at the lower-left corner of (A) is a SAED pattern from the sample. A representative TEM-EDS spectrum (point analysis) of the relatively Fe-rich area (C) and Mn-rich area (D) of vernadite nanophases. Cu peaks are from the carbon-coated TEM Cu grid that holds the specimen.

https://doi.org/10.1017/cmn.2024.17 Published online by Cambridge University Press

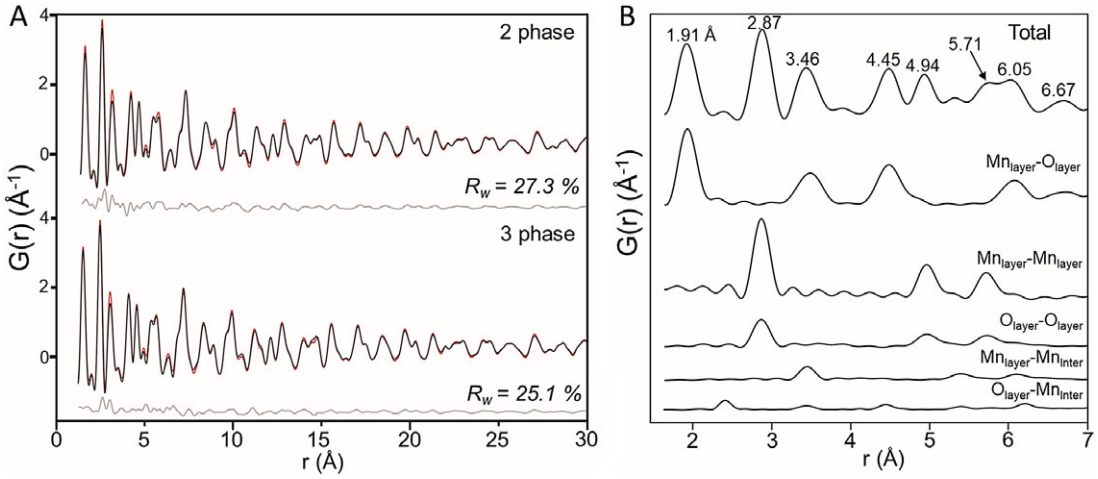

Figure 5. (A) PDF refinement of Fe-bearing vernadite phase from the outer layer of the HFMC using two phases (7 Å and 10 Å) and three phases (7 Å, 10 Å, and interstratified 7 Å/10 Å) from 1.6–30 Å ranges. The gray lines are differences between experimental (black) and calculated (red) PDF patterns. (B) The calculation of major atomic correlations from the refined vernadite structure (Table 1).

Mg, Si, Cl, K, Ca, Ti, Fe, Ni, and Zn (Fig. 4C,D). Ni and Mg are preferentially enriched in the Mn-rich area, while P is associated with the Fe-bearing area of vernadite nanomineral (Fig. 4C,D).

The detailed crystal structure of the vernadite nanophase was analyzed using the X-ray PDF technique (Fig. 5). In the PDF pattern, the first major peak at 1.90 Å corresponds to Mn–O correlations in the first shell of the Mn layer. The second peak at 2.86 Å refers to Mn–Mn and O–O correlations in the edge-sharing Mn octahedra. The mixture model of vernadite (Lee et al., 2019) is used for the PDF refinement, and the model consists of the 7 Å phase, the 10 Å phase, and the interstratified 7 Å/10 Å phases (Fig. 5; see also Fig. S4 in the Supplementary material). A comparison of the XRD and PDF patterns reveals that the sample does not include any 2-line or 6-line ferrihydrite as mechanical mixture (Fig. 6). If the iron is in the form of 2-line or 6-line ferrhydrite, the XRD pattern (Fig. 6A) will show a broad peak and shoulder at the low-angle side of the 2.43 Å and 1.41 Å peaks. The detection limit of synchrotron XRD can reach up to 0.01% by weight in crystalline mixtures (Thakral et al., 2018). As the TEM-EDS spectra also support the suggestion that Fe is incorporated into natural vernadite nanophases at HFMC (Fig. 4C,D), the Fe-bearing vernadite structure is used for the refinement. Yang et al. (2019a) reported the presence of Fe^{3+} in the vernadite from HFMC, as measured by electron energy loss spectroscopy (EELS) analysis.

Based on the weighted residue (R_w) values with parameters (Fig. 5A), the refined vernadite structure shows an acceptable agreement, and the results are listed in Table 1. Fe is involved in the Mn layer sites of the vernadite structure. We also tested the Fe^{3+} adsorbed on the vacancy sites of the vernadite structure, but it did not improve the goodness of fit. The Fe^{3+} could be incorporated into Mn layers of vernadite or adsorb the triple corner-sharing complex above or below vacancy sites of the octahedral sheet, which is similar to Mn^{3+} incorporated into both sites (Manceau et al.,

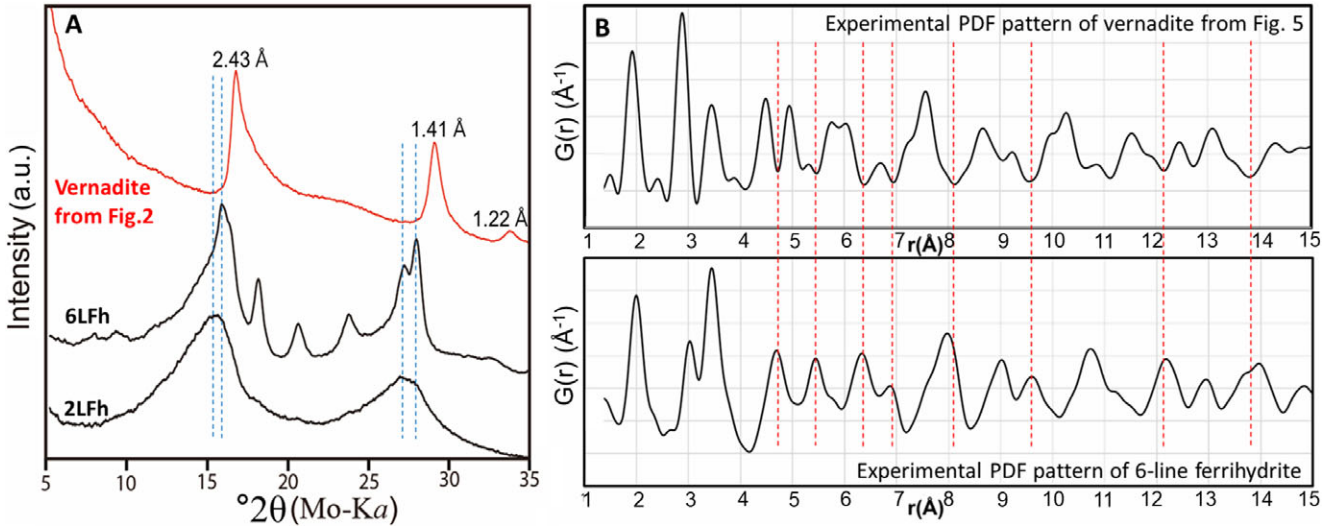

Figure 6. (A) Experimental XRD pattern of vernadite in HFMC compared with natural, 6-line ferrihydrite (6LFh) and 2-line ferrihydrite (2LFh), indicating that the vernadite sample does not have 2- or 6-line ferrihydrite as a mechanical mixture. Peaks and shoulders will be visible at the low-angle side of the 2.43 Å and 1.41 Å peaks in the XRD pattern if the iron-phase is present as 2- or 6-line ferrihydrite. (B) Experimental PDF patterns of vernadite and 6-line ferrihydrite. The vernadite PDF pattern shows valleys instead of peaks where ferrihydrite peaks would typically appear, indicating that the sample does not contain any 2-line or 6-line ferrihydrite as a mechanical mixture. Experimental XRD and PDF pattern of vernadite in HFMC compared with natural 6-line ferrihydrite (6LFh) and 2-line ferrihydrite (2LFh), indicating the vernadite.

https://doi.org/10.1017/cmn.2024.17 Published online by Cambridge University Press

Table 1. The structure of vernadite from two-phase PDF refinement of Fig. 5A

	x	*y*	*z*	$U_{11,22}$	U_{33}	Occ
7 Å vernadite (scale factor = 0.66)						
Mn	0	0	0	0.004 (4)	0.014 (4)	0.72 (3)
Fe	0	0	0	0.004 (4)	0.014 (4)	0.15 (5)
O	0.369 (3)	0	0.131 (8)	0.009 (5)	0.025 (8)	1.00 (1)
MnIL	0.672 (5)	0	0.316 (5)	0.025 (7)		0.15 (3)
OIL	0	0	0.5	0.029 (7)		0.15 (3)
NaIL	0.599 (5)	0	0.5	0.024 (8)		0.04
KIL	0.599 (5)	0	0.5	0.024 (8)		0.04
10 Å vernadite (scale factor = 0.25)						
Mn	0	0	0	0.012 (5)	0.018 (5)	0.76 (3)
Fe	0	0	0	0.012 (5)	0.018 (5)	0.11 (4)
O	0.349 (3)	0	0.102 (4)	0.020 (4)	0.025 (8)	1.00 (1)
MnIL	0.078 (2)	0	0.253 (4)	0.033 (8)		0.11 (3)
CaIL	0.078 (2)	0	0.253 (4)	0.033 (8)		0.05 (1)
MgIL	0.078 (2)	0	0.253 (4)	0.033 (8)		0.05 (1)
OIL	0.221 (5)	0	0.602 (8)	0.025 (6)		0.23 (5)

7 Å vernadite: *a*=4.962 (6) Å, *b*=2.833 (4) Å, *c*=7.20 (2) Å, β=97.3 (2)°; 10 Å vernadite: *a*=4.961 (6) Å, *b*=2.833 (4) Å, *c*=9.60 (4) Å, β=98.4 (3)°. U = isotropic displacement parameters, Occ = occupancy, IL = interlayer.

2013). The interlayer cations (i.e. Na^+, K^+, Ca^{2+}, and Mg^{2+}) were tested in PDF refinement and did not improve the fitting of the results. This suggests that this PDF analysis is not sensitive enough to precisely determine the interlayer cations in the vernadite structure (Zhu et al., 2012; Lee et al., 2019). During the PDF refinement, the mismatched residuals are mainly derived from the 2.87 Å and 3.46 Å peaks (Fig. 5). The mismatch could be caused by local distortions and aperiodic features of manganese octahedral layers (Xu et al., 2011).

Crystal chemistry

EPMA analyses were performed to determine the major element chemistry and elemental correlations of the HFMC (Fig. 7; see also Table S1 in the Supplementary material). Ca and Na are major elements in the vernadite interlayer and they correlate positively with Mn (Fig. 7A,B). The Fe/Mn ratios in the HFMC range from 0.31 to 0.69 (wt.% of atoms) and are negatively correlated (Fig. 7C). The lack of a link between Ca and P (Fig. 7D) suggests that Ca is not in the form of a phosphorus mineral (e.g. apatite). XRD patterns of HFMC also indicate that no phosphorus mineral is present in the sample. The absence of the phosphorus phases from the studied samples is also shown by the synchrotron XRD patterns of HFMC (Fig. 2). P and Fe have a positive correlation, while Ni and Co have a positive correlation with Mn (Fig. 7E–J). The atomic correlations observed among Mn, Fe, P, Ni, and Co are in agreement with the findings from the TEM-EDS analysis. (Fig. 4C,D). Similar to this, Hein et al. (2000) observed that Ni and Co are preferentially enriched in the Mn-rich HFMC.

Previous studies have shown the enrichment of REE in ferromanganese crusts from the Magellan Seamount in the northwest Pacific Ocean (Bolton et al., 1986; Hein et al., 2000; Jiang et al., 2011; Novikov et al., 2014). The total REE from the HFMC sample studied was plotted *vs* P in Fig. 8. The ΣREE has a positive correlation with P, indicating that phosphate and the REE concentrations are linked in the HFMC. The phosphate is positively correlated with Fe as evidenced by both the TEM-EDS (as shown in Fig. 4C,D) and the EPMA data analysis (Fig. 7D). This implies that Fe-rich vernadite might act as a host layer for the incorporation of phosphate, which in turn could locally enrich REE.

Several previous studies have reported the source and enrichment of PGE in the ferromanganese crusts (Hein et al., 2000; Ren et al., 2007; Hein and Koschinsky, 2014). The concentration of Pt can be enhanced up to 3000 ppb on the Pacific seamount HFMC. Furthermore, regions exhibiting an abundance of Pt are typically associated with hydrogenetic origins (Ren et al., 2007). The studied HFMC sample has Pt concentrations of up to 567.9 ppb and 629.26 ppb of ΣPGE, as also reported in previous studies by Sun et al. (2006) and Xue (2007). Plots of Pt *vs* Ni and Cu are shown from the inner to the outer side of the HFMC sample from the Magellan Seamount in Fig. 9. ΣPGE and Pt exhibit a positive correlation with Ni and Cu, according to Fig. 9. The correlation indicates that the platinum element exhibits similar behavior to copper and nickel during the formation of the HFMC. Hein et al. (2000) reported that PGE is correlated with siderophilic Co and Ni. In addition, the middle and inner parts are richer in Pt and ΣPGE (see Table S3 in the Supplementary material), which is likely due to the vernadite structure (i.e. 7 Å vernadite *vs* 10 Å vernadite, as shown in Fig. S4 of the Supplementary material). The inner part of the HFMC contains a greater quantity of 10 Å vernadite compared with 7 Å vernadite. Given that 10 Å vernadite possesses a larger interlayer gap than 7 Å vernadite, it might be more conducive to the incorporation of PGE (Lee et al., 2019).

The elemental correlations indicate that REE and P were more likely to be absorbed in the Fe-rich areas, while PGE, Co, and Ni were found to be more concentrated in the Mn-rich areas. These correlations align with previous geochemistry studies conducted on Fe-Mn crusts from the Magellan Seamounts (Glasby, 2006; Novikov and Bogdanova, 2007; Manceau et al., 2014) and Fe-Mn crusts from other localities (Xue, 2007; Zhang et al., 2009; Hein and Koschinsky, 2014; Yang et al., 2019b). The crystal structure and chemical composition of vernadite in HFMC may be the key factors that control the distribution of minor elements such as P, Ni, and Cu with trace elements (e.g. REE and PGE). Figure 10 consists of a schematic model of vernadite, highlighting the differences between the Fe-rich and Mn-rich areas in the vernadite.

The elemental correlations might also be influenced by the chemical hardness and softness of the metal cations and their associated ligands (Xu et al., 2017). The cations of REE are hard Lewis acids, which prefer to bind with a hard base like phosphate anions to form compounds like monazite (Ce, La, Nd)PO_4. The phosphorous tetrahedra at the Fe-bearing Mn layer help to build a strong bond with the REE, which could be crucial for the REE enrichment of HFMC (Fig. 10). The soft Lewis acids Cu, Co, Ni, and Pt cations establish strong covalent connections with the Mn(IV)-dominated octahedral layers of HFMC because Mn(IV) forms covalent bonds with nearby oxygen (Fig. 10). Pt can be adsorbed directly above the Mn octahdedra, similar to Cu in chalcophanite and Cu-adsorbed birnessite (Post and Appleman, 1988; Yang et al., 2019a).

Paleoclimatic records

The BSE images of a cross-section of the HFMC reveal chemical variations along the direction of growth at a microscopic scale

https://doi.org/10.1017/cmn.2024.17 Published online by Cambridge University Press

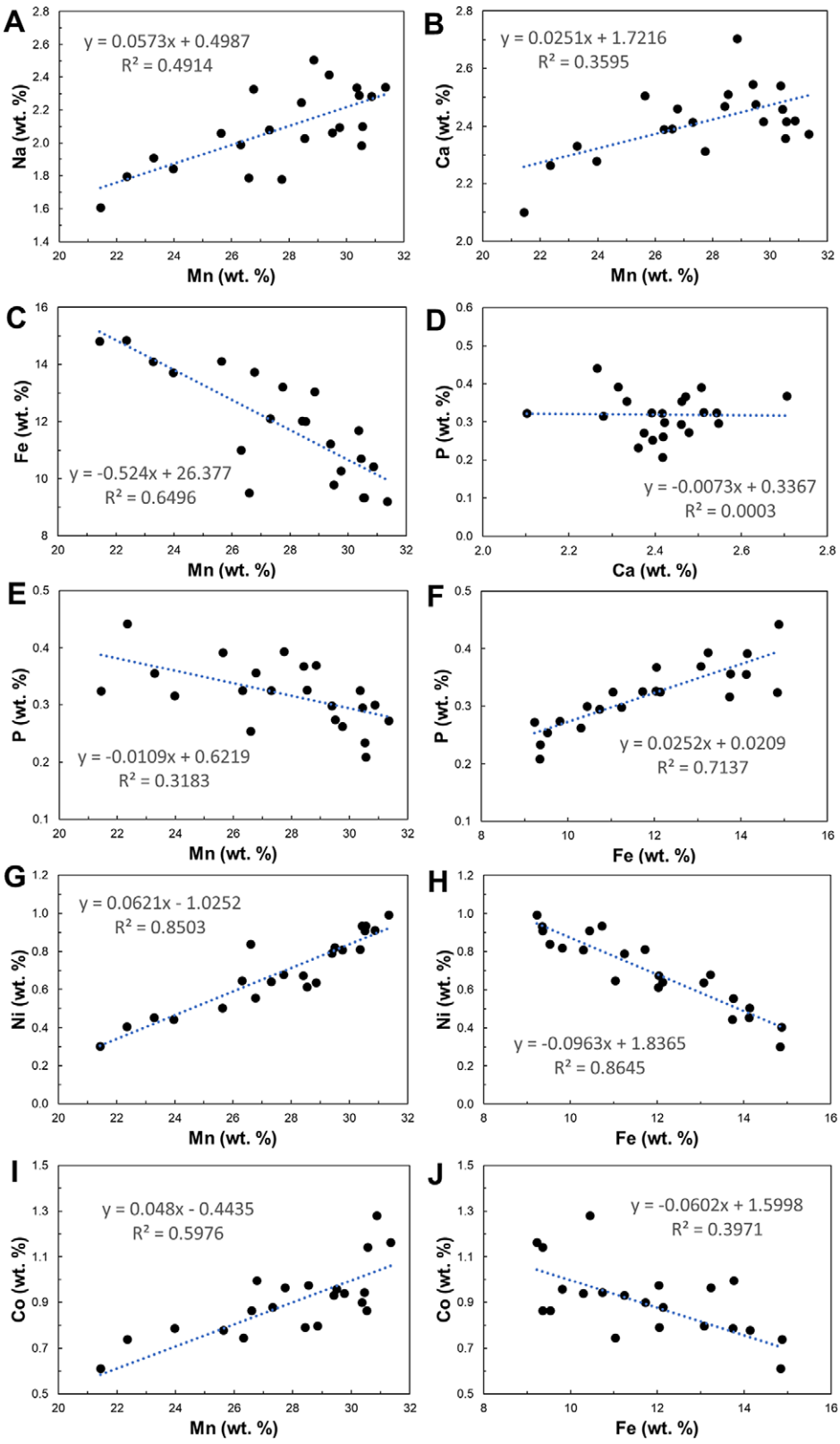

Figure 7. Plots of Na, Ca, Fe, P, Ni, and Co *vs* Mn and Fe from EMPA analyses of the outer part of HFMC. The full results of the major element analysis are shown in Table S1 in the Supplementary material.

(Fig. 11). The micro-bands display a variety of textures, alternating between columnar and botryoidal formations. Their thickness varies, ranging from less than a micron to several microns. The varied chemical characteristics of the microbands – such as their varying brightness in BSE mode – are connected to elements (e.g. Ni, Zn, Co, Na, Mg, Al, Si, P, S, Cl, K, Ca, and Ti) incorporated in the vernadite nanophases. The bands rich in Mn are linked with Mg and Ni, while the bands rich in Fe are associated

https://doi.org/10.1017/cmn.2024.17 Published online by Cambridge University Press

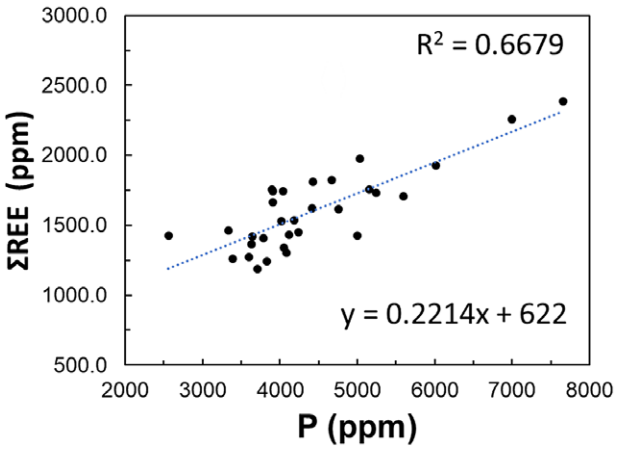

Figure 8. A plot of total REE *vs* P concentration of the studied HFMC, showing a positive correlation. The data are listed in Table S2 of the Supplementary material, reported by Xue (2007) and Zhang et al. (2009).

with P. This is based on the SEM elemental maps (as shown in Fig. 11D–H) and EDS spectra (see Fig. S5 in the Supplementary material). These findings align with the results from EPMA and TEM-EDS (Figs 4 and 7).

The paleoclimatic records were preserved by the HFMC, which crystallized from seawater that had undergone environmental and chemical changes over millions of years (Smith et al., 1989; Frank et al., 1999; Glasby et al., 2007; Lee and Xu, 2016). The age and associated geological occurrence of the HFMC from the Magellan Seamounts have been documented (Pulyaeva, 1997; Glasby et al., 2007; Melnikov and Pletnev, 2013). Pulyaeva (1997) and Melnikov and Pletnev (2013) recognized three units (I–III), based on the distribution of calcareous microfossils and benthic foraminiferal assemblages: layer I (inner part) in the Late Paleocene–Late Eocene, layer II (middle part) in the Middle Eocene–Late Miocene, and layer III (upper part) in the Pliocene and Quaternary. Three units are also present from the outside to the inner section of our examined HFMC sample (Fig. 1; see also Fig. S2 in the Supplementary material). As the outer part preserved the laminations (Fig. 11), this study focused on them to properly understand paleoclimatic changes.

The Magellan Seamounts HFMC average growth rate ranged from 1 to 3 mm Myr^{-1} (Glasby et al., 2007; Melnikov and Pletnev,

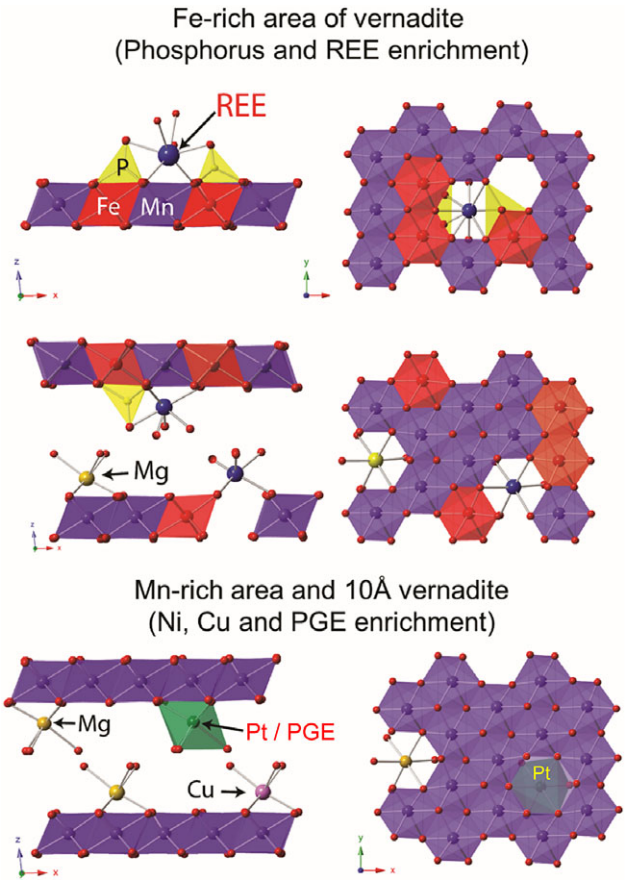

Figure 10. A schematic model for P, Ni, Cu, REE, and PGE enrichment of the vernadite structure between the Fe-rich area and the Mn-rich area. The Mn octahedral sites are shown in purple and the Fe octahedral sites in red.

2013). According to the Xue (2007) study, the outer portion of the HFMC sample that was examined in the study has a growth rate of 1.27 mm Myr^{-1}. This was determined by correlating the concentration of cobalt with the growth rate. There are various elemental fluctuations observed in the ferromanganese crust. Some areas, such as those depicted in Fig. 12A, maintain their texture from the top layer, making them suitable for paleoclimate research. Figure 12A shows the growth rate in relation to the ages of the

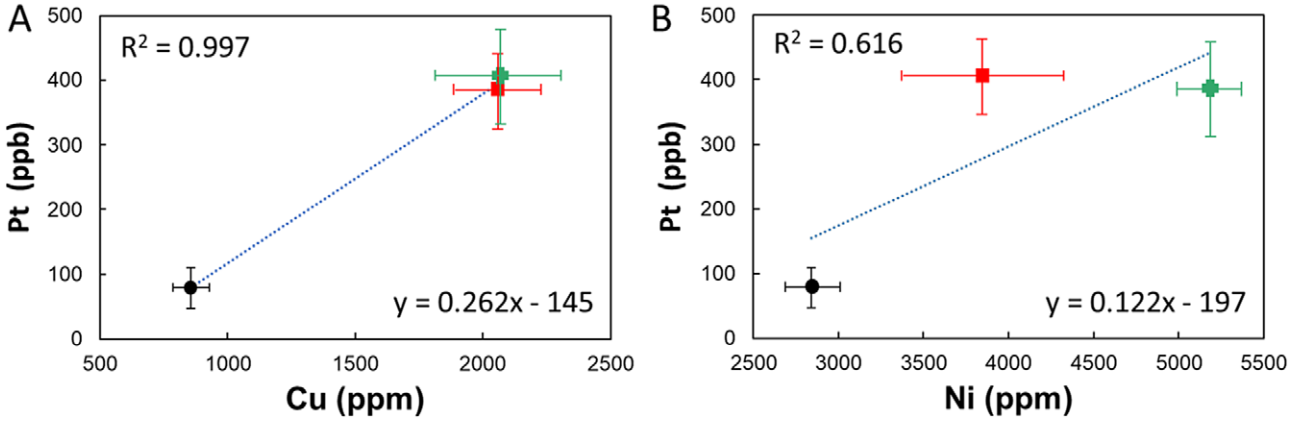

Figure 9. Plots of the average concentration of total Pt *vs* Ni and Cu of HFMC samples from the Magellan Seamount. The graph includes 232 data points: 75 in the outer part, 87 in the middle part, and 70 in the inner part. The data are listed in the Table S3 of the Supplementary material, as reported by Xue et al. (2005) and Sun et al. (2006). Black circle = outer part, red square = middle part, green cross = inner part.

https://doi.org/10.1017/cmn.2024.17 Published online by Cambridge University Press

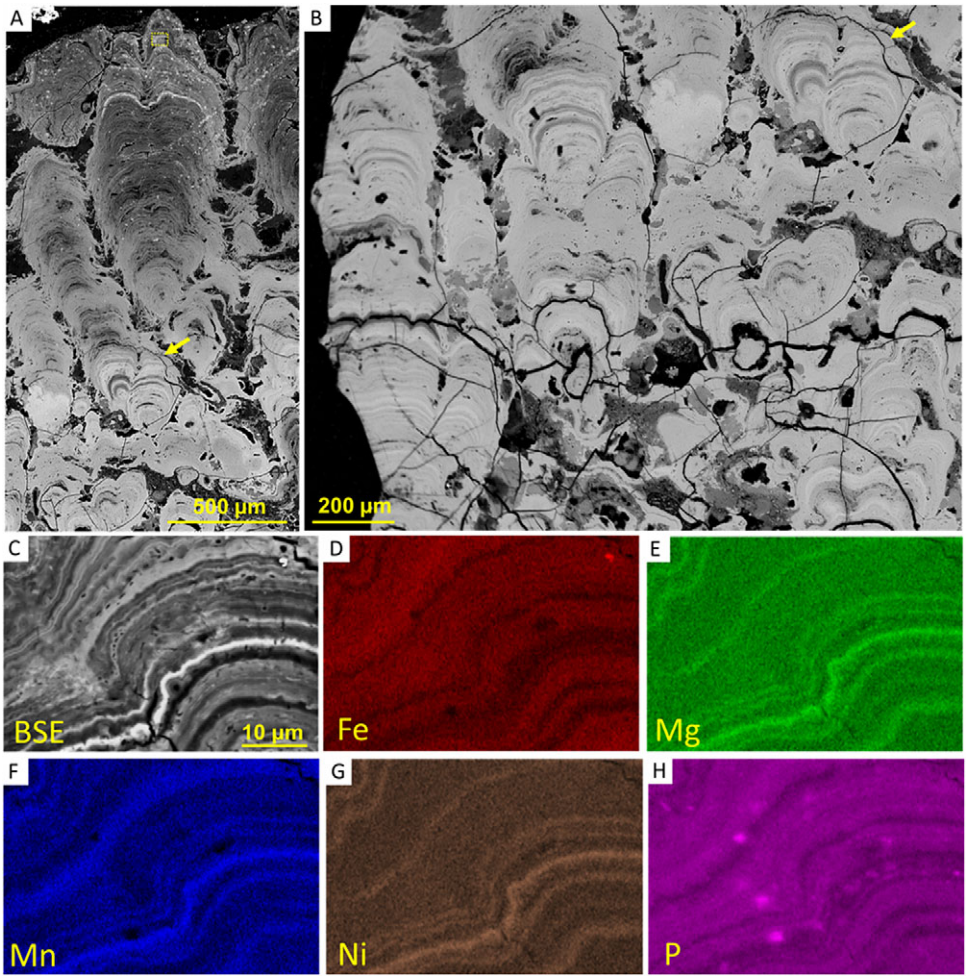

Figure 11. (A–C) The BSE images and (D–H) elemental maps from the studied HFMC sample. A small yellow box at top of the image (A) is the area for X-ray EDS mapping. (B) Enlarged images of the lower part of (A) indicated by a yellow arrow (C–H) showing oscillation of micro-sized layers along the growth direction. The bright layers in BSE images are related to the enrichment of Mn, Ni, and Mg.

HFMC layers. Furthermore, the layers and ages of the HFMC have been correlated with global sea levels, average global temperatures, and CO_2 concentrations dating back to 270,000 y ago. The bright layers (Ni-bearing Mn-rich bands) are highly correlated with the rise in global mean temperature, CO_2 concentrations, and sea level (Fig. 12B). The results suggest that the upper region of the HFMC is very responsive to changes in sea level and global temperature.

The oxygen minimum zone (OMZ) and dissolved oxygen concentration in seawater play a major role in controlling the growth and chemistry of the laminations in HFMC (Frank et al., 1999; Hein et al., 2000; Hein et al., 2013). In the OMZ, where it crosses with the oxidation of dissolved Mn^{2+} and oxygen-rich Antarctic water, a poorly crystalline vernadite phase is more likely to occur (Hein et al., 2013; Yang et al., 2019). The chemistry of the layers is associated with the redox shifts, or variations in the concentration of dissolved oxygen, which occur during the development of the HFMC. The rhythmic behavior of growth patterns suggests changes in the regional oceanographic setting, including the oxygen minimum zone and sea level, according to Marino et al. (2018). The Mn-rich vernadite bands (higher Mn/Fe ratio) originate in relatively oxidizing (more dissolved oxygen) environments, in contrast to the Fe- and P-bearing vernadite bands, which are formed in reducing environments (lower productivity of Mn(IV) oxide). Lu et al. (2005) reported on the chemical variations of layers of the Fe-Mn crust from the Central North Pacific region and found the drop in the Mn/Fe ratio linked with significant cooling events and a decrease in sea level.

The majority of earlier studies have revealed large-scale paleoclimatic periodic variation linked to the HFMC. Hein et al. (1992) found an association between composition variations with a million-year periodicity and changes in the ocean circulation pattern. Han et al. (2003), Ren et al. (2007), and Asavin et al. (2015) noted rhythmic variations in the Fe-Mn crust in the Western Pacific, which suggested that the 0.2–1.0 Myr cycles of chemical variations were controlled by Milankovitch cycles related to orbital eccentricity, obliquity, and precession, respectively. The cross-section of HFMC exhibits extremely small-scale compositional oscillations (sub-micron layers), which are related to millennial-scale paleoclimatic oscillations that took place during the Middle–Late Pleistocene and Holocene periods, including a glacial termination event (~126 kyr ago). These oscillations are visible in our high-resolution BSE images (Fig. 13). The observed 2 µm bands indicate cycles of ~1600 y, according to the growth rate (1.27 mm Myr^{-1}) derived from cobalt content (Fig. 13). Another HFMC sample (similar depth) that was taken from the Magellan Seamount regions similarly had fine-scale compositional

https://doi.org/10.1017/cmn.2024.17 Published online by Cambridge University Press

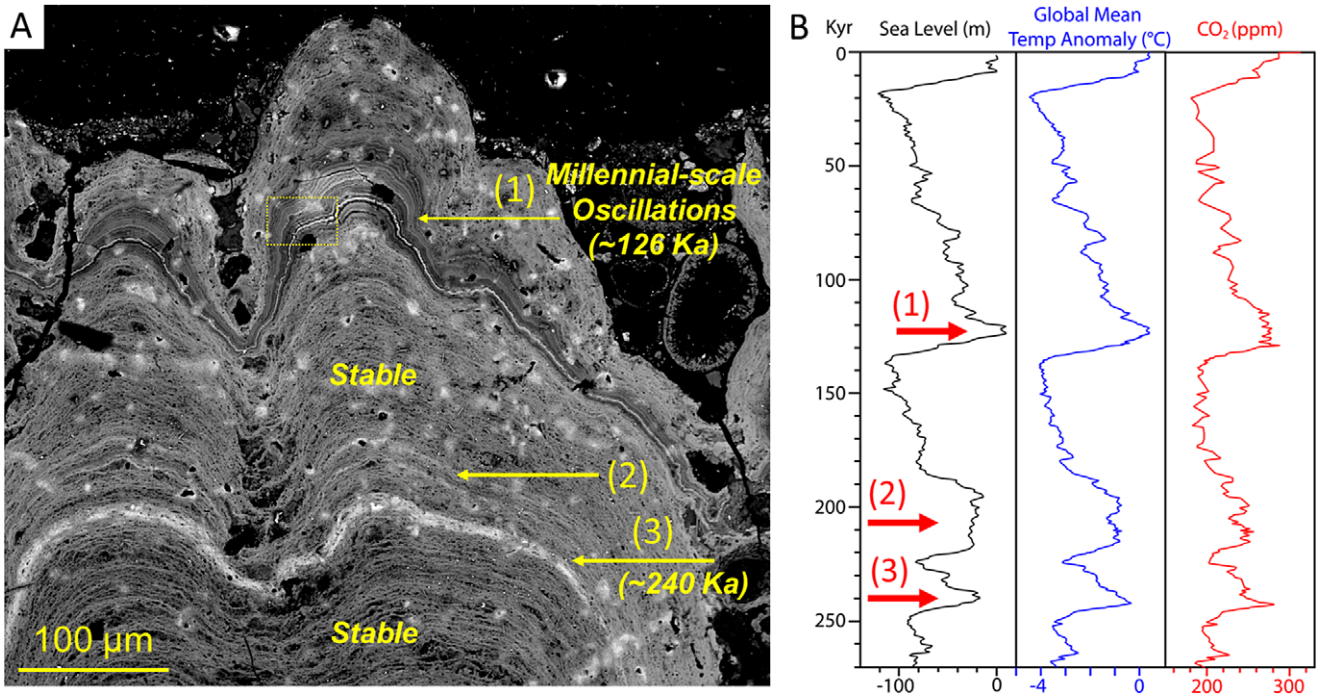

Figure 12. (A) The BSE image of the surfacial part of the HFMC sample linked to the ages based on the growth rates (1.27 mm Myr^{-1}). (B) The global sea level, global mean temperature, and CO_2 concentration for the past 270 kyr (modified from Hansen et al., 2007).

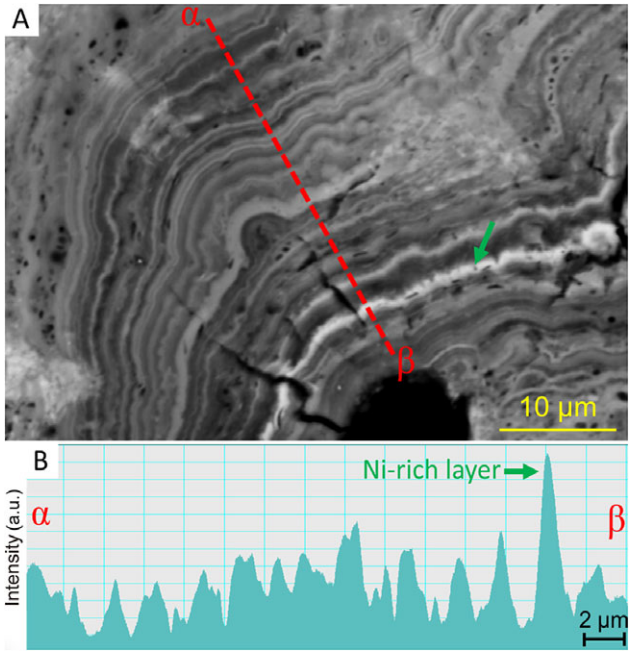

Figure 13. High-resolution BSE image of HFMC with intensity profile from α to β, indicating the sub-micron and micron-sized oscillating bands. (A) The area is a magnification of the yellow box in Fig. 12A. (B) The profile shows the ~2 μm intervals, indicating cycles of ~1600 y based on the growth rate (1.27 mm Myr^{-1}). The Ni-rich layer (corresponding to a glacial termination at ~126 kyr BP) is indicated by a green arrow.

oscillations in the outer section (same depth) (see Figs S1 and S6 in the Supplementary material).

Millennial-scale rapid climate changes for the Pleistocene and Holocene epochs have been widely reported in sediments, ice cores, and submarine anoxia (Dansgaard et al., 1993; Bond et al., 1997; Hyodo et al., 2017). There was also a series of rapid millennial-scale climatic variations during the last glacial era, according to Turney et al.'s (2004) interpretation of peat humification investigations. In the deep-ocean environment, rhythmically interbedded limestone and marl layers revealed millennial-scale climatic oscillations (<2100 y) (Elrick and Hinnov, 1996). Despite the characteristics being observed in many marine sediments, glacial deposits, and terrestrial deposits, the causes of such millennial-scale climate variability are still not fully understood (Elrick and Hinnov, 1996; Clark et al., 1999). This is due to limitations in the resolution of the chronology, poor preservation, and additional variations, including those caused by local climatic, oceanographic, tectonic, geographic, and biological factors. Several studies suggest that the millennial paleoclimatic changes are mainly caused by ice sheet melting modulated by solar activity contributing to the global climate system (Elrick and Hinnov, 1996; Bond et al., 1997; Turney et al., 2004; Wang et al., 2005; Hyodo et al., 2017). Ice-sheet growth and decay may be related to fine-scale paleoclimatic variations found in our examined HFMC samples (Figs 11–13). The slow growth rates and HFMC sensitivity to variations in sea level are key factors in recording fine-scale paleoclimatic changes. More ferromanganese crusts from other sites, depths, and sources need to be examined in future studies in order to understand the fine-scale paleoclimate variations.

Conclusions

The combination of XRD, PDF, SEM, and TEM techniques is useful for examining the crystal chemistry and structure of poorly crystallized nanominerals such as vernadite (Lee et al., 2016; Lee and Xu, 2016; Yang et al., 2018). In the HFMC, vernadite plays a key role in accumulating PGE, REE, and critical metals such as Co and Ni. A detailed chemical analysis shows that PGE, Co, and Ni are mainly found in the Mn-rich vernadite. On the other hand,

https://doi.org/10.1017/cmn.2024.17 Published online by Cambridge University Press

REE and P are likely to be absorbed by the Fe-rich vernadite. The formation and chemical variation of HFMC layers are controlled by redox changes in the oxygen minimum zone associated with global sea level fluctuations and glacial periods. We observed millennia-scale paleoclimatic oscillations at the uppermost layer of the HFMC. Fine-scale chemical oscillations that exhibit cycles of ~1600 y during the Middle–Late Pleistocene and Holocene periods are present, including a glacial termination event (~126 kyr ago). An increase in the Mn/Fe ratio of the HFMC layer is associated with the glacier melting period. The micro-bands in HFMC could be a valuable indicator for paleoclimatic changes, because they are sensitive to oxygen levels in dissoved seawater. Further research on HFMC samples from various places, depths, and sources is needed to better understand both long-term and short-term paleoclimatic changes.

Supplementary material. The supplementary material for this article can be found at http://doi.org/10.1017/cmn.2024.17.

Author contribution. Lee carried out most of the experimental work and data analysis, and drafted the manuscript. Xu conceived the idea, acquired research funding, supervised the project, prepared the samples, carried out some of the experimental works and data analysis, and contributed to manuscript writing.

Data availability statement. The datasets used and analyzed during the current study are available from the corresponding author on reasonable request.

Acknowledgements. The authors thank Professor Xiaoming Sun and Dr Ting Xue for providing the sample. The authors gratefully acknowledge use of facilities and instrumentation supported by NSF through the University of Wisconsin Materials Research Science and Engineering Center (DMR-1720415), and the advance photon source is a U.S. Department of Energy (DOE) Office of Science User Facility operated for the DOE Office of Science by Argonne National Laboratory under contract no. DE-AC02-06CH11357.

Financial support. This work was supported by the NASA Astrobiology Institute (NNA13AA94A) and by the National Research Foundation of Korea (NRF) grant funded by the Korea government (MSIT) (No.RS-2024-00342773).

Competing interests. The authors declare that they have no known competing financial interests or personal relationships that could have appeared to influence the work reported in this paper.

References

Asavin, A. M., Daryin, A. V., & Melnikov, M. E. (2015). Microrhythmic distribution of Co, Mn, Ni, and La contents in cobalt-rich ferromanganese crusts from the Magellan Seamounts. *Geochemistry International*, *53*, 19–38.

Berezhnaya, E., Dubinin, A., Rimskaya-Korsakova, M., & Safin, T. (2018). Accumulation of platinum group elements in hydrogenous Fe–Mn crust and nodules from the Southern Atlantic Ocean. *Minerals*, *8*, 275.

Bolton, B., Ostwald, J., & Monzier, M. (1986). Precious metals in ferromanganese crusts from the south-west Pacific. *Nature*, *320*, 518.

Bond, G., Showers, W., Cheseby, M., Lotti, R., Almasi, P., DeMenocal, P., Priore, P., Cullen, H., Hajdas, I., & Bonani, G. (1997). A pervasive millennial-scale cycle in North Atlantic Holocene and glacial climates. *Science*, *278*, 1257–1266.

Cheng, Z., Shi, X., Su, X., Chen, Z., Wu, Y., Li, X., Ju, X., Yang, Y., & Shi, F. (2005). Biostratigraphy, growth period and sedimentary environment of ferromanganese crusts from Magellan Seamounts in the Western Pacific. *Advances in Marine Science*, *23*, 422–430.

Clark, P.U., Webb, R.S., & Keigwin, L.D. (1999). *Mechanisms of Global Climate Change at Millennial Time Scales*, pp. 59–76. American Geophysical Union, Washington.

Cronan, D.S. (1999). *Handbook of Marine Mineral Deposits*, pp 239–273. CRC Press, Boca Raton.

Dansgaard, W., Johnsen, S., Clausen, H., Dahl-Jensen, D., Gundestrup, N., Hammer, C., Hvidberg, C., Steffensen, J., Sveinbjörnsdottir, A., & Jouzel, J. (1993). Evidence for general instability of past climate from a 250-kyr ice-core record. *Nature*, *364*, 218.

Du, D., Yan, S., Yang, F., Zhu, Z., Song, Q., & Yang, G. (2018). Kriging interpolation for evaluating the mineral resources of cobalt-rich crusts on Magellan Seamounts. *Minerals*, *8*, 374.

Elrick, M., & Hinnov, L.A. (1996). Millennial-scale climate origins for stratification in Cambrian and Devonian deep-water rhythmites, western USA. *Palaeogeography, Palaeoclimatology, Palaeoecology*, *123*, 353–372.

Farrow, C., Juhas, P., Liu, J., Bryndin, D., Božin, E., Bloch, J., Proffen, T., & Billinge, S. (2007). PDFfit2 and PDFgui: computer programs for studying nanostructure in crystals. *Journal of Physics: Condensed Matter*, *19*, 335219.

Frank, M., O'Nions, R., Hein, J., & Banakar, V. (1999). 60 Myr records of major elements and Pb–Nd isotopes from hydrogenous ferromanganese crusts: reconstruction of seawater paleochemistry. *Geochimica et Cosmochimica Acta*, *63*, 1689–1708.

Glasby, G.P. (2006). Manganese: predominant role of nodules and crusts. *Marine Geochemistry*, pp. 371–427. Springer, Berlin.

Glasby, G.P., Ren, X., Shi, X., Pulyaeva, I.A. (2007). Co-rich Mn crusts from the Magellan Seamount cluster: the long journey through time. *Geo-Marine Letters*, *27*, 315–323.

Grangeon, S., Fernandez-Martinez, A., Claret, F., Marty, N., Tournassat, C., Warmont, F., & Gloter, A. (2017). In-situ determination of the kinetics and mechanisms of nickel adsorption by nanocrystalline vernadite. *Chemical Geology*, *459*, 24–31.

Han, X., Jin, X., Yang, S., Fietzke, J., & Eisenhauer, A. (2003). Rhythmic growth of Pacific ferromanganese nodules and their Milankovitch climatic origin. *Earth and Planetary Science Letters*, *211*, 143–157.

Hansen, J., Sato, M., Kharecha, P., Russell, G., Lea, D.W., & Siddall, M. (2007). Climate change and trace gases. *Philosophical Transactions of the Royal Society A*, *365*, 1925–1954.

Hein, J.R., & Koschinsky, A. (2014). Deep-ocean ferromanganese crusts and nodules. *Treatise on Geochemistry*, *2*, 273–291

Hein, J.R., Koschinsky, A., Bau, M., Manheim, F.T., Kang, J.-K., & Roberts, L. (2000). Cobalt-rich ferromanganese crusts in the Pacific. *Handbook of marine mineral deposits*, pp. 239–273. CRC Press, Boca Raton, Florida, USA.

Hein, J.R., Mizell, K., Koschinsky, A., & Conrad, T.A. (2013). Deep-ocean mineral deposits as a source of critical metals for high-and green-technology applications: comparison with land-based resources. *Ore Geology Reviews*, *51*, 1–14.

Hein, J. R., Bohrson, W. A., Schulz, M. S., Noble, M., & Clague, D. A. (1992). Variations in the fine-scale composition of a Central Pacific ferromanganese crust: paleoceanographic implications. *Paleoceanography*, *7*, 63–77.

Hyodo, M., Bradák, B., Okada, M., Katoh, S., Kitaba, I., Dettman, D.L., Hayashi, H., Kumazawa, K., Hirose, K., & Kazaoka, O. (2017). Millennial-scale northern Hemisphere Atlantic-Pacific climate teleconnections in the earliest Middle Pleistocene. *Scientific Reports*, *7*, 10036.

Pan, J., De Carlo, E., Yi, Y., Liu, S., & You, G (2005). Effect of phosphatization on element concentration of cobalt-rich ferromanganese crusts. *Acta Geological Sinica*, *79*, 349–355.

Jiang, X., Lin, X., Yao, D., & Guo, W. (2011). Enrichment mechanisms of rare earth elements in marine hydrogenic ferromanganese crusts. *Science China: Earth Sciences*, *54*, 197–203.

Juhás, P., Davis, T., Farrow, C.L., & Billinge, S.J. (2013). PDFgetX3: a rapid and highly automatable program for processing powder diffraction data into total scattering pair distribution functions. *Journal of Applied Crystallography*, *46*, 560–566.

Koppers, A.A., Morgan, J.P., Morgan, J.W., & Staudigel, H. (2001). Testing the fixed hotspot hypothesis using 40Ar/39Ar age progressions along seamount trails. *Earth and Planetary Science Letters*, *185*, 237–252.

Koppers, A.A., Staudigel, H., Wijbrans, J.R., Pringle, M.S. (1998). The Magellan seamount trail: implications for Cretaceous hotspot volcanism and absolute Pacific plate motion. *Earth and Planetary Science Letters*, *163*, 53–68.

Lee, S., Shen, Z., & Xu, H. (2016). Study on nanophase iron oxyhydroxides in freshwater ferromanganese nodules from Green Bay, Lake Michigan, with implications for the adsorption of As and heavy metals. *American Mineralogist*, *101*, 1986–1995.

Lee, S., & Xu, H. (2016). XRD and TEM studies on nanophase manganese oxides in freshwater ferromanganese nodules from Green Bay, Lake Michigan. *Clays and Clay Minerals*, *64*, 523–536.

Lee, S., Xu, H., Xu, W., & Sun, X. (2019). The structure and crystal chemistry of vernadite in ferromanganese crusts. *Acta Crystallographica, Section B*, *75*, 591–598.

Lu, Z., Ling, H., Zhou, F., Jiang, S., Chen, X., & Zhou, H. (2005). Variation of the Fe/Mn ratio of ferromanganese crusts from the cetral North Pacific: implication for paleoclimate changes. *Acta Petrolei Sinica*, *15*, 530–537.

Manceau, A., Lanson, M., & Takahashi, Y. (2014). Mineralogy and crystal chemistry of Mn, Fe, Co, Ni, and Cu in a deep-sea Pacific polymetallic nodule. *Amercian Mineralogist*, *99*, 2068–2083.

Manceau, A., Marcus, M.A., Grangeon, S., Lanson, M., Lanson, B., Gaillot, A.-C., Skanthakumar, S., & Soderholm, L. (2013). Short-range and long-range order of phyllomanganate nanoparticles determined using high-energy X-ray scattering. *Journal of Applied Crystallography*, *46*, 193–209.

Marino, E., González, F., Lunar, R., Reyes, J., Medialdea, T., Castillo-Carrión, M., Bellido, E., & Somoza, L. (2018). High-resolution analysis of critical minerals and elements in Fe–Mn crusts from the Canary Island Seamount Province (Atlantic Ocean). *Minerals*, *8*, 285.

Melnikov, M., & Pletnev, S. (2013). Age and formation conditions of the Co-rich manganese crust on guyots of the Magellan seamounts. *Lithology and Mineral Resources*, *48*, 1–13.

Novikov, G., & Bogdanova, O.Y. (2007). Transformations of ore minerals in genetically different oceanic ferromanganese rocks. *Lithology and Mineral Resources*, *42*, 303–317.

Novikov, G., Mel'nikov, M., Bogdanova, O.Y., & Vikent'ev, I. (2014). Nature of co-bearing ferromanganese crusts of the Magellan Seamounts (Pacific Ocean): Communication 1. Geology, mineralogy, and geochemistry. *Lithology and Mineral Resources*, *49*, 1–22.

Post, J. E., & Appleman, D. E., 1988). Chalcophanite, $ZnMn_3O_7{\cdot}3H_2O$; new crystal–structure determinations. *American Mineralogist*, *73*, 1401–1404.

Pulyaeva, I. (1997). Stratification of ferromanganese crusts on the Magellan. *Marine Geology Palaeoceanography*, pp. 111–128. CRC Press, Beijing.

Ren, X., Glasby, G., Liu, J., Shi, X., & Yin, J. (2007). Fine-scale compositional variations in a Co-rich Mn crust from the Marcus-Wake Seamount cluster in the western Pacific based on electron microprobe analysis (EMPA). *Marine Geophyscial Research*, *28*, 165–182.

Smith, W.H., Staudigel, H., Watts, A.B., Pringle, M.S. (1989). The Magellan Seamounts: Early Cretaceous record of the South Pacific isotopic and thermal anomaly. *Journal of Geophysical Research: Solid Earth*, *94*, 10501–10523.

Sun, X., Xue, T., He, G., Ye, X., Zhang, M., Lu, H., & Wang, S. (2007). Noble gas isotopic compositions of cobalt-rich ferromanganese crusts from the western Pacific Ocean and their geological implications. *Acta Petrolei Sinica*, *81*, 90–98.

Sun, X., Xue, T., He, G., Zhang, M., Shi, G., ShengWei, W., & Lu, H. (2006). Platinum group eleemtns (PGE) and OS isotopic geochemistry of ferromangane crusts from Pacific Ocean seamounts and their constriants on genesis. *Acta Petrolei Sinica*, *22*, 3014–3026.

Thakral, N. K., Zanon, R. L., Kelly, R. C., & Thakral, S. (2018). Applications of powder X-ray diffraction in small molecule pharmaceuticals: achievements and aspirations. *Journal of Pharmaceutical Sciences*, *107*, 2969–2982.

Toby, B.H., & Von Dreele, R.B. (2013). GSAS-II: the genesis of a modern open-source all purpose crystallography software package. *Journal of Applied Crystallography*, *46*, 544–549.

Turney, C.S., Kershaw, A.P., Clemens, S.C., Branch, N., Moss, P.T., & Fifield, L. K. (2004). Millennial and orbital variations of El Nino/Southern Oscillation and high-latitude climate in the last glacial period. *Nature*, *428*, 306.

Wang, Y., Cheng, H., Edwards, R.L., He, Y., Kong, X., An, Z., Wu, J., Kelly, M.J., Dykoski, C.A., & Li, X. (2005). The Holocene Asian monsoon: links to solar changes and North Atlantic climate. *Science*, *308*, 854–857.

Xu, H., Xu, D.C., & Wang, Y. (2017). Natural indices for the chemical hardness/softness of metal cations and ligands. *ACS Omega*, *2*, 7185–7193.

Xu, W., Hausner, D.B., Harrington, R., Lee, P.L., Strongin, D.R., & Parise, J.B. (2011). Structural water in ferrihydrite and constraints this provides on possible structure models. *American Mineralogist*, *96*, 513–520.

Xue, T. (2007). Geochemiscal characters and Ore-forming elements enrichment mechanism of ferromanganese crust from pacific ocean. PhD Dissertation, Sun Yat-Sen University.

Xue, T., Xiaoming, S., Gaowen, H., Shengwei, W., Hongfeng, L., & Mei, Z. (2005). Geochemistry of PGE and Au in ferromanganese crusts from seamounts in the west Pacific Ocean. *Mineral Deposit Research: Meeting the Global Challenge*, pp. 207–209. Springer, Berlin.

Yang, K., Park, H., Son, S.-K., Baik, H., Park, K., Kim, J., Yoon, J., Park, C.H., & Kim, J. (2019a). Electron microscopy study on the formation of ferromanganese crusts, western Pacific Magellan Seamounts. *Marine Geology*, *410*, 32–41.

Yang, P., Lee, S., Post, J.E., Xu, H., Wang, Q., Xu, W., & Zhu, M. (2018). Trivalent manganese on vacancies triggers rapid transformation of layered to tunneled manganese oxides (TMOs): implications for occurrence of TMOs in low-temperature environment. *Geochimica et Cosmochimica Acta*, *240*, 173–190.

Yang, P., Post, J. E., Wang, Q., Xu, W., Geiss, R., McCurdy, P. R., & Zhu, M. (2019b). Metal adsorption controls stability of layered manganese oxides. *Environmental Science & Technology*, *53*, 7453–7462.

Zhang, M., Sun, X., Xue, T., Liu, S., He, G., & Lu, H. (2009). REE geochemistry of ferromanganese crusts from west Pacific Ocean and its geological implications. *Mineral Deposits*, *28*, 111–122.

Zhu, M., Farrow, C.L., Post, J.E., Livi, K.J., Billinge, S.J., Ginder-Vogel, M., & Sparks, D.L. (2012). Structural study of biotic and abiotic poorly-crystalline manganese oxides using atomic pair distribution function analysis. *Geochimica et Cosmochimica Acta*, *81*, 39–55.

https://doi.org/10.1017/cmn.2024.17 Published online by Cambridge University Press